J. Fluid Mech. (2007), *vol.* 577, *pp.* 137–159.
doi:10.1017/S0022112007004624 Printed in the United Kingdom

On the formation and propagation of nonlinear internal boluses across a shelf break

SUBHAS K. VENAYAGAMOORTHY
AND OLIVER B. FRINGER

Environmental Fluids Mechanics Laboratory, Department of Civil and Environmental Engineering, Stanford University, Stanford, CA 94305-4020, USA

(Received 1 May 2006 and in revised form 16 October 2006)

High-resolution two- and three-dimensional numerical simulations are performed of first-mode internal gravity waves interacting with a shelf break in a linearly stratified fluid. The interaction of nonlinear incident waves with the shelf break results in the formation of upslope-surging vortex cores of dense fluid (referred to here as internal boluses) that propagate onto the shelf. This paper primarily focuses on understanding the dynamics of the interaction process with particular emphasis on the formation, structure and propagation of internal boluses onshelf. A possible mechanism is identified for the excitation of vortex cores that are lifted over the shelf break, from where (from the simplest viewpoint) they essentially propagate as gravity currents into a linearly stratified ambient fluid.

1. Introduction

The subject of internal waves interacting with bottom topographic features in the ocean has received much attention in the past few decades. This is mainly attributed to a proposition that instabilities and breaking of internal waves at boundaries can be a significant source of turbulence, leading to mixing and transport in the ocean (Munk & Wunsch 1998). There are a number of mechanisms through which turbulence can be generated when flow interacts with topography, such as lee wave generation, tidal–topographic generation of internal waves, internal wave reflection and internal wave scattering (Kunze & Llewellyn Smith 2004). Of these mechanisms, critical reflection and scattering of internal waves are the primary mechanisms that lead to the transfer of energy toward smaller scales leading to turbulent dissipation and mixing. Although it is far from clear which of these mechanisms is most important, it is postulated that the critical reflection of internal waves could perhaps be the most efficient process in generating turbulence (Kunze & Llewellyn Smith 2004). New field measurements taken over a continental slope suggest that critical reflection is a key mechanism for channelling low-mode internal wave energy to smaller scales and turbulence (Nash *et al.* 2004).

In a linearly stratified fluid (i.e. of a constant buoyancy frequency N), a first-mode internal wave (or in general any wave mode) propagating in a fluid of finite depth over flat topography with horizontal boundaries can be described as a superposition of pairs of phase-locked upward and downward propagating beams, which are characterized by both horizontal and vertical wavenumbers k and m and frequency ω (for a detailed discussion, see Thorpe 1999). For a first-mode incident wave interacting with a sloping bottom (figure 1), the presence of the slope

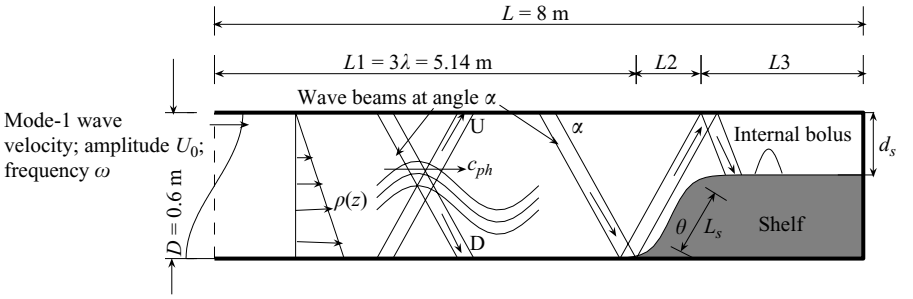

FIGURE 1. Schematic diagram showing the computational domain and set-up used in simulations for this study. A mode-one internal wave is imposed at the left-hand boundary of the domain with frequency $\omega = 0.33\ \mathrm{rad\,s^{-1}}$ and wavelength $\lambda = 2\pi/k = 1.713\ \mathrm{m}$. The horizontal length $L2$ of the slope and the onshelf water depth d_s are varied to obtain a range of slope angles θ such that the slope length $L_s = D = 0.6\ \mathrm{m}$ is kept constant for all runs. The onshelf length $L3$ is varied such that the overall length $L = 8\ \mathrm{m}$. The schematic also shows the decomposition of the wave mode into a pair of upward (U) and downward (D) propagating beams. For clarity, only the reflection of the downward propagating beam is extended to the slope region. Non-dimensional parameters: $\gamma/s = \tan\theta/\tan\alpha$; $Fr = U_0/c$; $Fr_E = U_0T/(\pi L_s)$; d_s/D.

effectively decouples the upward and downward propagating wave beams (Thorpe 1987), permitting the description of the interaction of modes with a sloping boundary using internal wave beams. Internal wave beams exhibit simple but peculiar reflection patterns at boundaries compared to waves in optics and acoustics. Unlike in optics and acoustics, where the angles of incidence and reflection are preserved with respect to the normal of the reflecting surface (classical Snell's law), internal waves preserve their angle with respect to the direction of gravity upon reflection (Phillips 1977). This implies that the incident beams preserve their frequency on reflection. From this property, it is easy to show that the slope, s, of the internal wave beam (or characteristic) is given by

$$s = \tan\alpha = \frac{k}{m} = \left(\frac{\omega^2 - f^2}{N^2 - \omega^2}\right)^{1/2}, \tag{1.1}$$

where α is the angle of the internal wave characteristic with respect to the horizontal plane and f is the sine of latitude Coriolis parameter. Bottom slopes are then readily classified by the ratio γ/s (Phillips 1977), where γ is the topographic slope. Subcritical slopes ($\gamma/s < 1$) correspond to topographic slopes that are flat compared to the wave characteristic slope, whereas supercritical slopes ($\gamma/s > 1$) correspond to topographic slopes that are steeper than the wave characteristic slope. Critical slopes ($\gamma/s = 1$) correspond to waves in which the angle of propagation of the group velocity (or energy) matches the topographic slope, leading to focusing of wave energy and hence enhanced dissipation and mixing in the bottom boundary layer. It should be noted that the ratio of the incoming wave frequency, ω, to the critical wave frequency, ω_c, for a given topography can also be used to classify the slope. However, in what follows we use the ratio γ/s, as it is more commonly used in oceanographic literature.

Several laboratory experiments have been performed to study incident internal waves on a slope (Cacchione & Wunsch 1974; Ivey & Nokes 1989; Taylor 1993; Ivey, Winters & De Silva 2000; Dauxois, Didier & Falcon 2004). These experiments demonstrate the principles of internal wave reflection and clearly show the development of a turbulent boundary layer for a critical slope. Observations were made of an upslope-surging bolus (a vortex of dense fluid or thermal front as

termed by Thorpe 1992) that resulted when the waves overturned and broke onslope. Numerical studies of the interaction of incident internal wave rays with a slope were carried out by Slinn & Riley (1998), and the results indicate the formation of the upslope-surging bolus and highlight the complexity of the interaction process. In all the previous laboratory experimental studies, the upslope-surging boluses were trapped at the apex of the wedge-shaped region, leading to enhanced dissipation and mixing. There are also numerous theoretical studies on linear and weakly nonlinear internal wave interactions with slopes (e.g. Craig 1985; Thorpe 1987; Dauxois & Young 1999).

In this paper, we describe results from highly-resolved laboratory-scale numerical simulations of the interaction of highly nonlinear first-mode internal waves with a shelf break. We present results showing the formation of upslope-surging boluses in the slope region consistent with results from previous studies. The energetics of the interaction process is of fundamental interest and has been addressed extensively by Venayagamoorthy & Fringer (2005, 2006). However, the focus of this paper is the formation, propagation and fate of internal boluses over a shelf break. Our motivation for this study comes from observations of highly nonlinear bottom-trapped internal waves of elevation in coastal regions (Klymak & Moum 2003; Carter, Gregg & Lien 2005). Such observed highly nonlinear bottom-trapped internal waves are probably prime candidates for mass and sediment transport.

The layout of this paper is as follows. In § 2, we briefly discuss the computational approach we employ for this study and provide an overview of the problem set-up. We present results of the interaction process and conditions under which internal boluses form in § 3. We follow with a discussion of the structure and propagation of internal boluses onshelf in § 4, with conclusions given in § 5.

2. Governing equations and computational approach

We adapt the Navier–Stokes equations with the Boussinesq approximation given by

$$\frac{\partial \boldsymbol{u}}{\partial t} + \boldsymbol{u}\cdot\nabla\boldsymbol{u} = -\frac{1}{\rho_0}\nabla p + \nu\nabla^2\boldsymbol{u} - \frac{g}{\rho_0}\rho\boldsymbol{k}, \tag{2.1}$$

$$\frac{\partial \rho}{\partial t} + \nabla\cdot(\rho\boldsymbol{u}) = \kappa\nabla^2\rho, \tag{2.2}$$

$$\nabla\cdot\boldsymbol{u} = 0, \tag{2.3}$$

where ν is the (constant) kinematic viscosity and κ is the (constant) scalar diffusivity. Equations (2.1)–(2.3) are computed with the large-eddy simulation (LES) code developed by Fringer & Street (2003) in the two-dimensional domain shown in figure 1 (the three-dimensional simulations use a lateral width $W = 0.5$ m). This code employs the fractional-step method of Zang, Street & Koseff (1994) to solve the Navier–Stokes and scalar transport equations presented in equations (2.1)–(2.3) using a finite-volume formulation on a generalized curvilinear coordinate non-staggered grid with a rigid lid. This code has been extensively validated with a number of different laboratory-scale studies on geophysical fluid dynamics using its single-processor version (Zang & Street 1995; Zedler & Street 2001; Fringer & Street 2003) as well as its parallel version (Cui & Street 2001, 2004).

For all the simulations, the initial stratification is given by the background distribution $\rho_b(z)$, which is linear and is given by

$$\frac{\rho(z, t=0)}{\rho_0} - 1 = \frac{\rho_b(z)}{\rho_0} = -\frac{\Delta\rho}{\rho_0}\left(\frac{z}{D}\right), \tag{2.4}$$

with $\Delta\rho/\rho_0 = 0.02$, which results in a buoyancy frequency of $N = 0.57$ rad s^{-1} in a depth of $D = 60$ cm. At the left-hand boundary of the domain shown in figure 1, we impose a first-mode internal wave given by

$$u(0, z, t) = U_0 \cos(mz)\sin(\omega t), \tag{2.5}$$

where U_0 is the velocity amplitude of the forcing, m is the vertical wavenumber corresponding to a mode-1 baroclinic wave with $m = \pi/D$, ω is the forcing frequency, and u is the cross-shore velocity component. Boundary conditions for the cross-shore (horizontal) velocity u are no-slip on the bottom boundary, free-slip at the top boundary, and no-flux at the right boundary. The vertical velocity has a no-flux boundary condition at both top and bottom boundaries, and free-slip boundary conditions on all other walls, and the density field has a gradient-free boundary condition on all walls. The grid size is 512×128 for the two-dimensional runs and $512 \times 32 \times 128$ for the three-dimensional runs, with a maximum Courant number of 0.2. We use a kinematic viscosity of $\nu = 10^{-5}$ m^2 s^{-1}, and a thermal diffusivity of $\kappa = 10^{-6}$ m^2 s^{-1}, which gives a Prandtl number of $Pr = 10$. A rough estimate of the turbulent Reynolds number for these flows, based on an advective length scale of $L_c = U_0/\omega = 0.13$ m and a characteristic overturning velocity of $U_0 = 4$ cm s^{-1}, is $Re_T = 500$. The corresponding Kolmogorov microscale is then $\eta_k = L_c Re_T^{-3/4} = 1.17$ mm. With a longitudinal grid spacing of 15.6 mm and vertical grid spacings of 4.7 mm in the deep region and 1.6 mm in the shallow region, the longitudinal grid spacing is about 15 times larger than the Kolmogorov microscale and the largest vertical grid spacing is 3 times larger.

The important non-dimensional parameters (as also shown previously by, e.g. Legg & Adcroft 2003; Kunze & Llewellyn Smith 2004) for this problem (in a finite-depth domain) include the ratio of the topographic slope to the internal wave characteristic slope, γ/s, and the non-dimensional steepness of the incoming wave (a measure of the wave amplitude), which we define here as a Froude number, $Fr = U_0/C_{ph}$. Here, U_0 is the maximum velocity amplitude and C_{ph} is the linear first-mode internal wave speed in a linearly stratified fluid given by (Kundu 1990)

$$c_{ph} = \frac{\omega}{k} = \frac{D}{\pi}(N^2 - \omega^2)^{1/2}. \tag{2.6}$$

The third relevant non-dimensional parameter $Fr_E = U_0 T/(\pi L_s)$, where $T = 2\pi/\omega$ is the wave period, gives a measure of the wave excursion to the topographic length scale, L_s. Another important parameter is the ratio of the onshore to offshore water depths, d_s/D, which provides a measure of the amplitude of the topography, $h_t = D - d_s$, relative to the offshore water depth, D. In this study, the variation in the topographic slope γ is achieved by changing the topographic amplitude h_t. It is not trivial to obtain different values of γ/s without altering either $(D - d_s)/D$ or changing the frequency of the incoming wave field (which would imply changing the incoming wave properties).

While holding N and ω, and hence s, fixed, we carried out a series of simulations with different topographic slopes, γ, such that γ/s varied from 0 to 1.5 and covered a broad range of sub- and supercritical slopes. We also varied the velocity amplitude,

Runs	γ/s	$Fr = U_0/c_{ph}$	$U_0T/(\pi L_s)$	h_t/D	Comments
1–10	0.25–1.5	0.06	0.05	0.17–0.72	Linear cases
11–20	0.25–1.5	0.11	0.10	0.17–0.72	Linear cases
21–30	0.25–1.5	0.45	0.41	0.17–0.72	Nonlinear cases
31–40	0.25–1.5	0.78	0.71	0.17–0.72	Highly nonlinear cases
41–60	0.5–1.5	0.22–0.67	0.20–0.61	0.57	Intermediate *Fr* runs
61	1	0.78	0.71	0.57	Three-dimensional run on a critical slope

TABLE 1. List of simulations performed showing the parameter space covered, with $T = 2\pi/\omega$.

U_0, between $0.5\,\mathrm{cm\,s^{-1}}$ to $7\,\mathrm{cm\,s^{-1}}$, in order to vary the Froude number, $Fr = U_0/c_{ph}$, which ranged from 0.056 to 0.783. This yielded a parameter space that allowed us to assess the conditions under which wave breaking and the subsequent formation of internal boluses occur. Table 1 gives the parameter space covered by the simulations.

3. Interaction and generation dynamics onslope

In this section, we provide a discussion of the flow fields in the slope region, as well as the formation of boluses, using results mainly from two-dimensional simulations shown in table 1. The three-dimensional results are presented to show the lateral instabilities as well as to validate the two-dimensional simulation results on which the bulk of the discussion in this paper is based.

3.1. *Wave–slope interaction*

The interaction of incoming highly nonlinear first-mode internal waves with a critical slope is shown in figure 2 using a time sequence of the density field over two wave periods from a two-dimensional simulation. Figure 3 shows the interaction obtained from a three-dimensional simulation for the same case and time sequence as shown in figure 2. The discussion below refers to both of these figures and we find that the two-dimensional dynamics are qualitatively similar to the three-dimensional results. However, a quantitative comparison will require three-dimensional simulations at more realistic Reynolds numbers, where strong three-dimensional instabilities and turbulence are more likely to occur. In figure 3(*a*), the density isopycnals dip close to the slope as the long incident wave interacts with it. Soon afterward, the isopycnals steepen further, leading to wave breaking as shown in figure 3(*b*), causing the density contours to fold up even further resulting in the formation of a front around which the wave overturns (figure 3*b*, *c*), consistent with observations made in laboratory experiments by Dauxois *et al.* (2004) and Ivey & Nokes (1989). The overturned lump of fluid surges upslope as the flow oscillates back upslope as shown in figure 3(*d*). The strong distortion of the isopycnals leads to wave breaking and generation of vortices, which we discuss later (see figure 20) along with the presence of vortex cores in the slope region using a three-dimensional simulation. The surging bolus of fluid travels over the shelf break and is propelled onto the shelf as shown in figure 3(*e*) as a blob of dense fluid, which we refer to as an internal bolus. This bolus then propagates shoreward (see figure 3(*f*) onwards). Meanwhile, the process repeats itself as a new wave arrives at the slope (at $t/T = 5.6$). However, as new waves arrive, the wave field is complicated as a result of the interaction of the incoming waves with those that are reflected from the slope. The fold-up of the isopycnals is intensified even further owing to more intense wave breaking as shown in figure 3(*f*, *g*). Heavy fluid is still transported upslope and internal boluses continue to form (although they

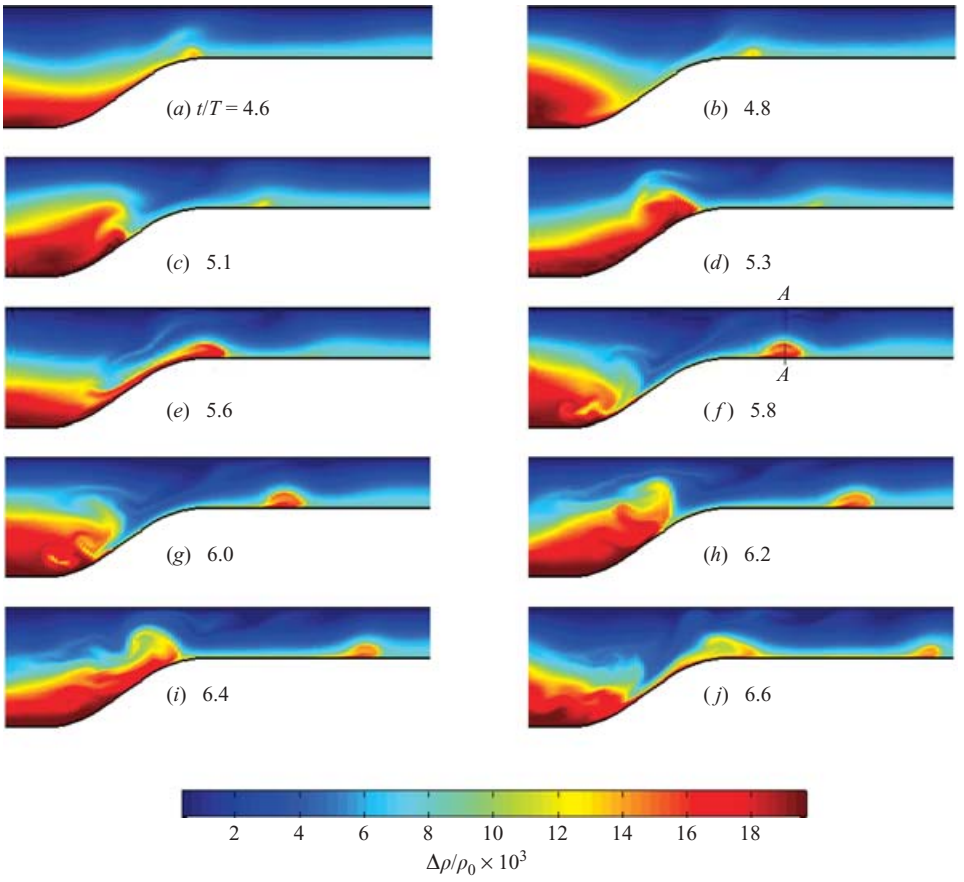

FIGURE 2. Density field (shown in colour) of an internal wave interacting with a critical slope for a highly nonlinear case with $Fr = 0.783$, showing how the internal bolus forms and propagates onshore (to the right) as a result of the interaction process (see figure 16 for detail of the bolus core shown in section A–A). For clarity, only the right-hand half of the computational domain from $x = 4.8$ to 6.9 m is shown and time is normalized by the wave period $T = 19.2$ s.

are not as dense as the earlier one) and propagate onshelf as seen in figure 3(i, j). Based on these observations, we anticipate that the dissipation in the slope region will increase owing to the modified reflection processes that seem to occur as a result of the interaction between incident and reflected waves with the slope. We will be addressing the dissipation and irreversible mixing that occurs in the slope and shelf regions in detail via further three-dimensional simulations in a subsequent paper.

We gain a better perspective of the breaking process and the upslope movement of the dense bolus by superimposing the velocity vectors over the density field in the slope region as shown in figure 4, where the flow field is shown over one wave period from $t/T = 4.6$ to $t/T = 5.6$. In figure 4(a), the flow is essentially offslope. As this flow relaxes and then reverses towards the slope (figure 4b, c), the isopycnals steepen at the leading edge of the wave, with a strong reverse flow in the bottom boundary layer owing to heavy fluid still descending from upslope. As the flow toward the slope accelerates, the local fluid velocity exceeds the phase velocity (i.e. $U > c_{ph}$), setting up local kinematic instabilities that cause wave breaking, thus leading to entrainment of

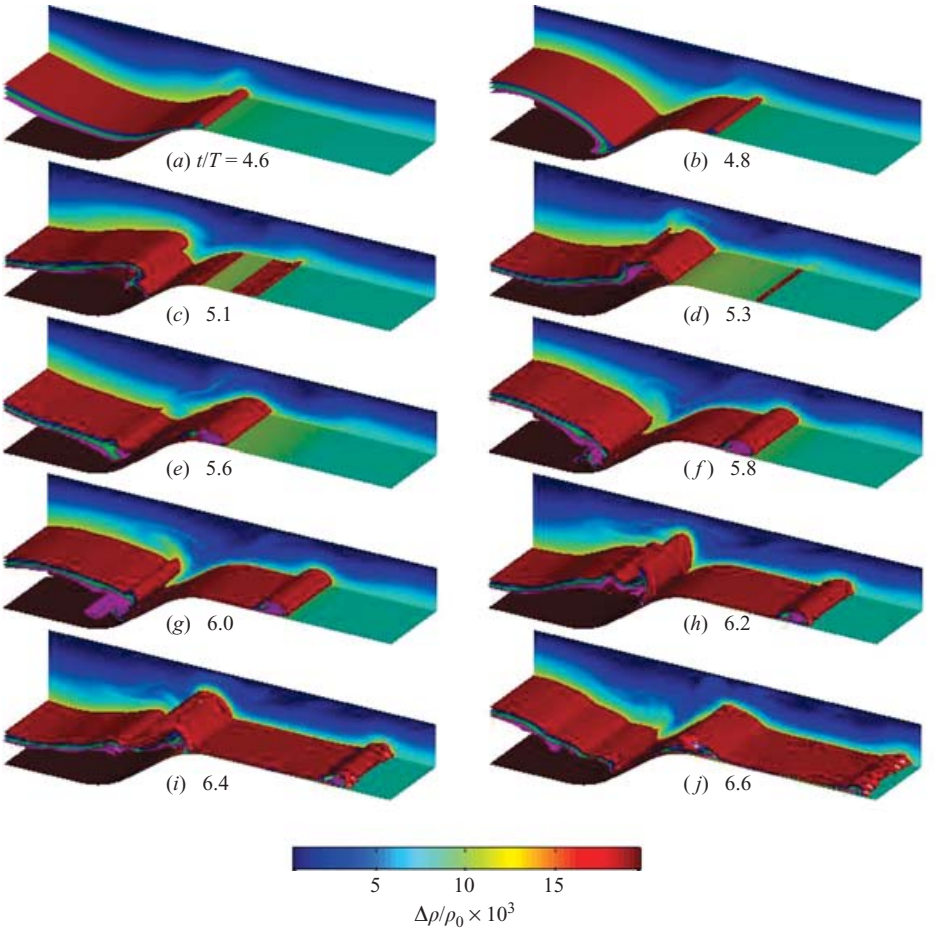

FIGURE 3. Three-dimensional density isosurfaces of an internal wave with $Fr = 0.783$ interacting with a critical slope. These results are from a three-dimensional simulation of the two-dimensional case shown in figure 2. For clarity, only the right-hand half of the domain from $x = 4.6$ to 6.9 m is shown and time is normalized by the wave period $T = 19.2$ s. The isosurface values are $\Delta\rho/\rho_0 = 0.0115, 0.0125, 0.0135$ and 0.0145, respectively, and the sideline plane shows the density field as indicated by the colour bar.

light fluid beneath the heavy fluid (figure 4*c*, *d*). The incoming wave accelerates the flow in the bottom boundary layer which results in the upslope surge of heavy fluid (figure 4*e*).

The presence of the slope compresses the horizontal flow field associated with the wave leading to strong vertical accelerations resulting in a highly non-hydrostatic flow field. A modal analysis of velocity fields in the slope region is performed to determine the nature of the wave field in the vicinity of slope region, and this is discussed in § 3.2. As the flow relaxes (figure 4*f*), the head of the front continues to move upslope and the emergence of the internal bolus is seen in figure 4(*g*) at the shelf break. Notice the strong rotation around the bolus. The bolus separates as the return flow increases in strength in the bottom boundary layer. The process essentially repeats itself (the time sequence is not shown here), however as alluded to in our discussion of figure 2, the breaking process intensifies and increases the stirring and dissipation

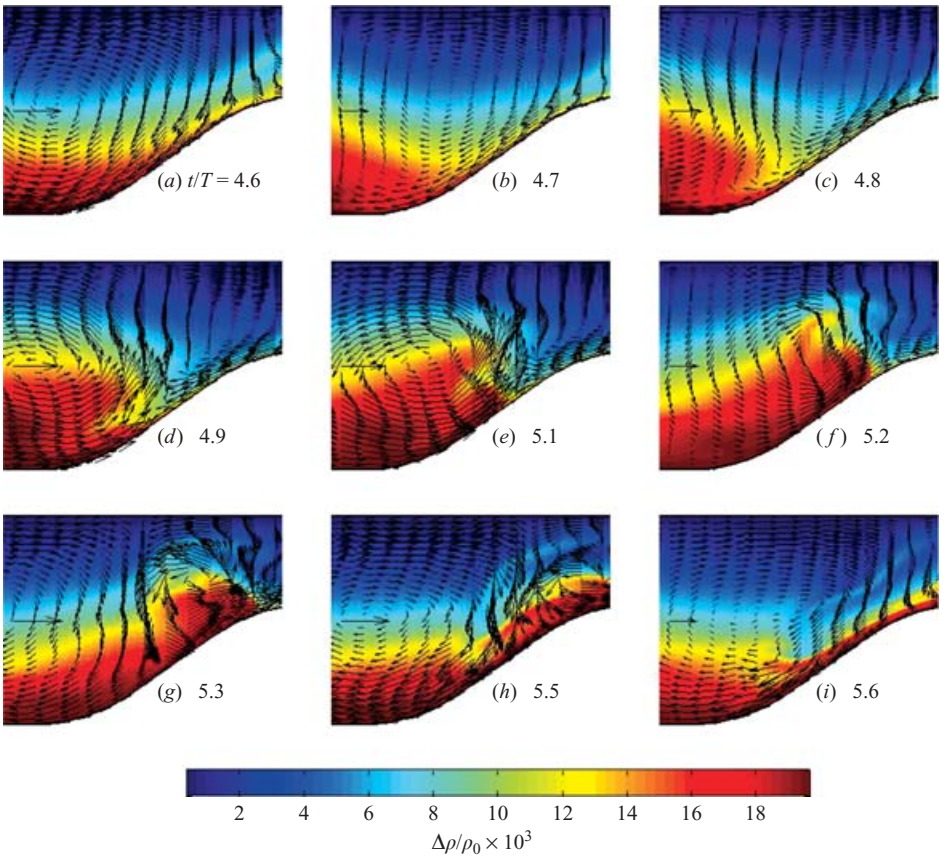

FIGURE 4. Velocity vectors superimposed over the density contours to show the interaction dynamics of the flow induced by the wave field with the slope. This figure shows enlarged details of the slope region shown in figure 2, over one wave period (from $t/T = 4.6$ to 5.6). The magnitude of the single horizontal velocity vector in the left-hand centre on each panel is $7\,\mathrm{cm\,s^{-1}}$, corresponding to the maximum forcing velocity amplitude of the incident wave imposed at the left-hand boundary. Waves propagate from left to right, and every fourth velocity vector is depicted for clarity.

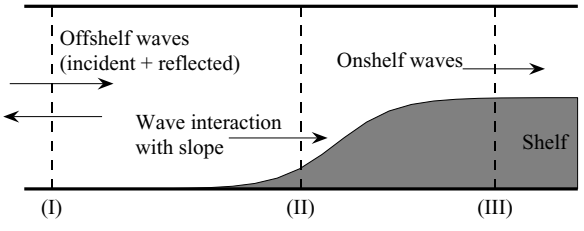

FIGURE 5. Schematic diagram showing the locations where the EOF analysis is performed. Section (I) is 4.6 m from the left-hand boundary, section (II) is at midslope and section (III) is at the shelf break.

close to the slope. Hence, the resulting internal bolus seen onshelf in figure 2(j) is not as dense as the earlier bolus depicted in figure 2(e).

3.2. *Modal analysis*

To understand better how the incoming wave field is modified as a result of the interaction with the slope, and to determine the nature of the reflected as well as the

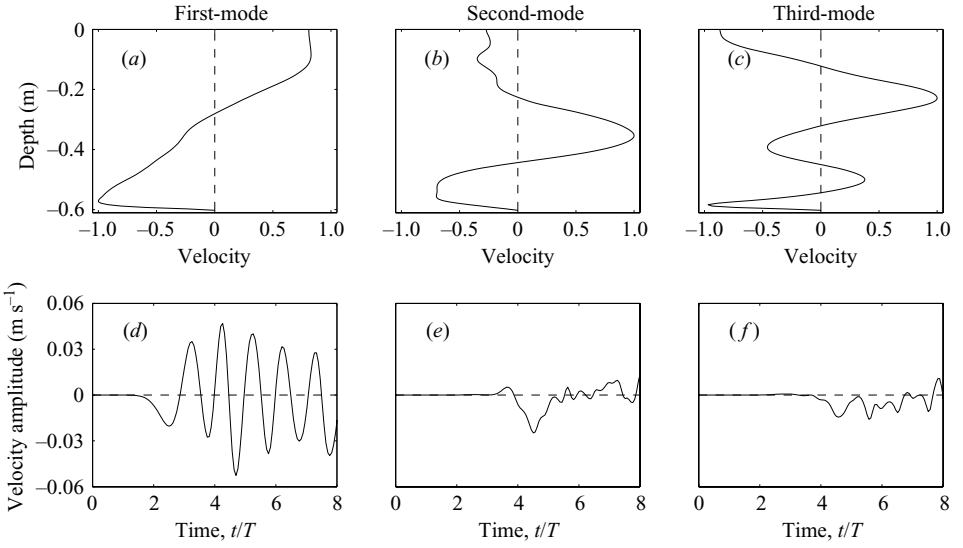

FIGURE 6. Horizontal velocity profiles and amplitudes for the three lowest modes at section (I) from the EOF analysis.

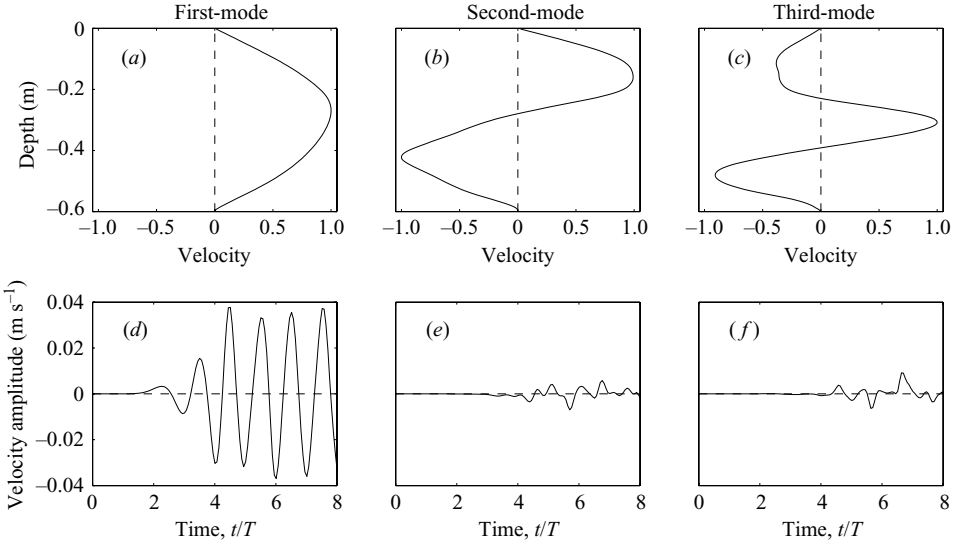

FIGURE 7. Vertical velocity profiles and amplitudes for the three lowest modes at section (I) from the EOF analysis.

transmitted waves, we employ a modal analysis of the velocity fields using empirical orthogonal functions (EOF). This technique is conventionally used in oceanography for analysing datasets of space–time distributed observations (Borzelli & Ligi 1999). For the present study, this approach is attractive since the standard normal modes analysis is not suitable because of the highly nonlinear nature of the flow field. In the EOF procedure used for this study, a matrix containing the simulation data at each vertical section is formed and the time mean removed from each time series. The eigenvalues and corresponding eigenvectors (or 'EOFs') of the covariance matrix are then calculated. The 'EOFs' corresponding to the largest eigenvalues

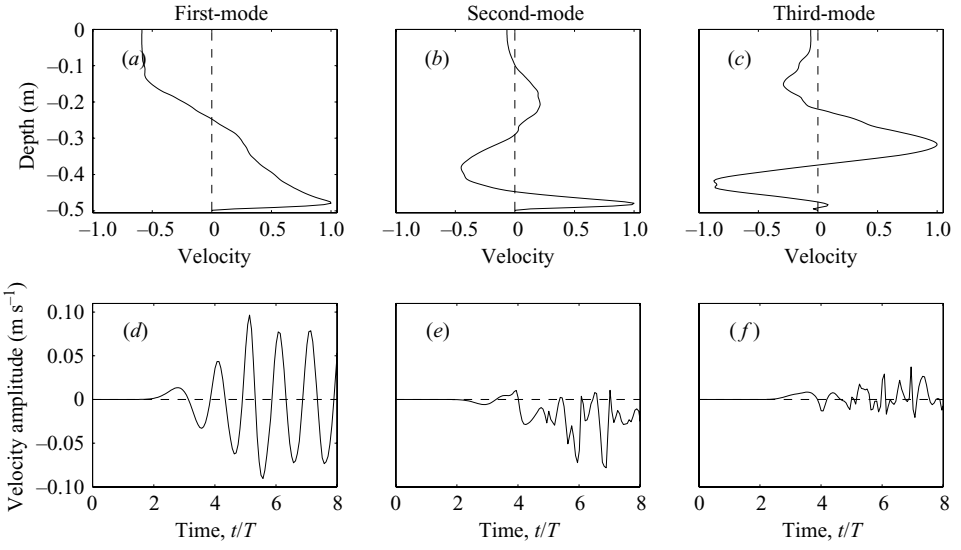

FIGURE 8. Horizontal velocity profiles and amplitudes for the three lowest modes at section (II) from the EOF analysis.

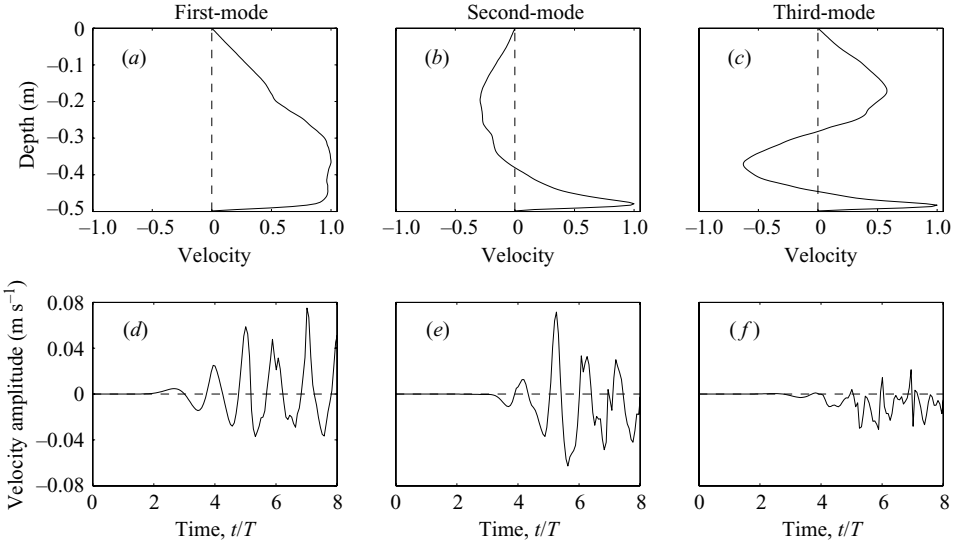

FIGURE 9. Vertical velocity profiles and amplitudes for the three lowest modes at section (II) from the EOF analysis.

represent the shapes of the lowest 'modes'. We analysed the velocity data at the three locations shown in figure 5, for the highly nonlinear first-mode internal wave case with $Fr = 0.783$ interacting with a critical slope as shown in figures 2–4, so as to determine the nature of the wave modes at these locations.

The empirical orthogonal functions (EOFs) or 'modes' corresponding to the three largest eigenvalues as well as the time series of the amplitudes are shown in figures 6–11, for both the horizontal and vertical velocity fields at sections (I), (II) and (III), respectively. At section (I) (figures 6–7), the flow is almost entirely mode-one, even later in time when incoming waves and reflected waves interact with one another.

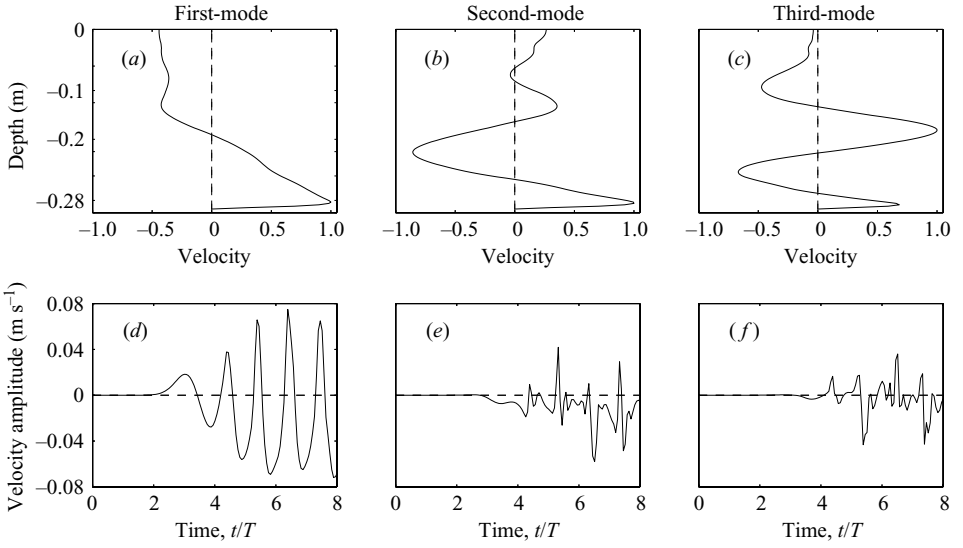

FIGURE 10. Horizontal velocity profiles and amplitudes for the three lowest modes at section (III) from the EOF analysis.

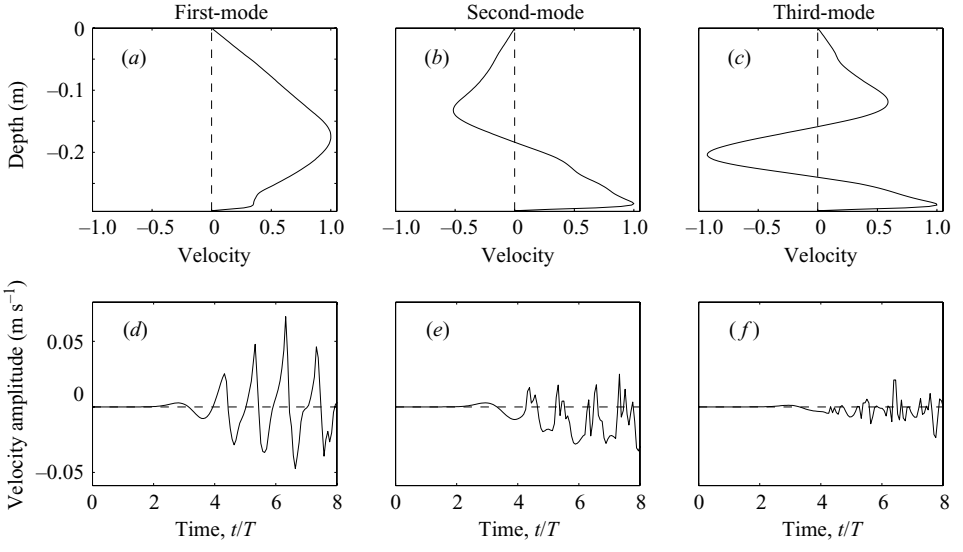

FIGURE 11. Vertical velocity profiles and amplitudes for the three lowest modes at section (III) from the EOF analysis.

The contributions from the other two modes are negligible, as can be seen from both the vertical velocity amplitudes and the percentage contributions of the higher modes to the total variance of the vertical velocity shown in figure 12(*b*). At section (II) (midslope region), the generation of higher modes and their contributions are no longer small as shown in figures 8–9. The contributions from the second-mode are significant, as can be seen from the amplitudes of both velocity components as well as the contributions to the total variances shown in figure 12. The high velocities observed at the lower boundary in the slope region in figure 4 have a strong contribution from the second-mode. On the shelf (section (III)), the presence of the higher modes is

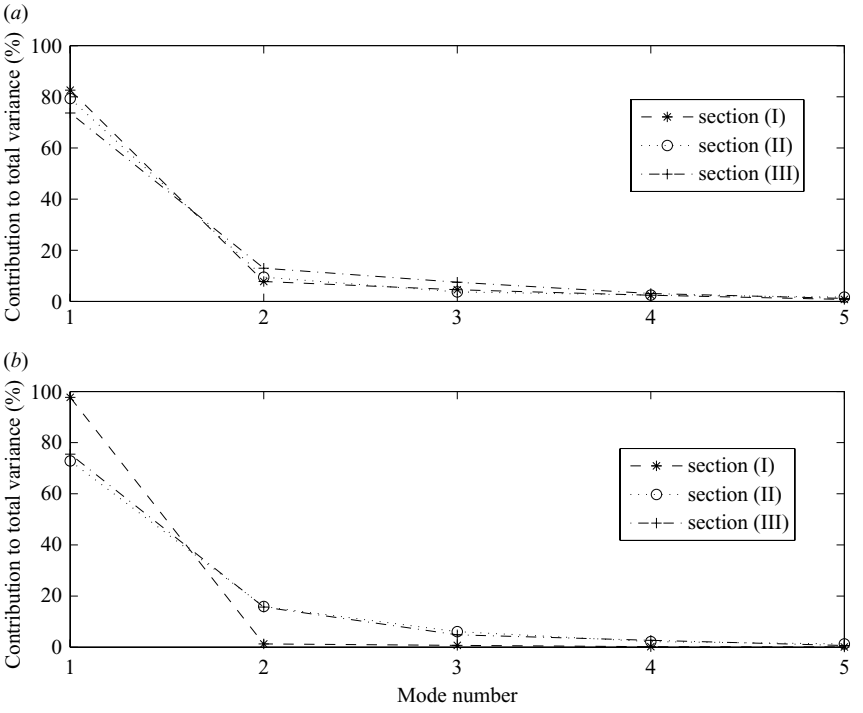

FIGURE 12. Percentage contributions of the lowest five modes to the total variance in the EOF analysis. (*a*) horizontal velocity; (*b*) vertical velocity.

clearly seen by the amplitude signal of the velocity modes (see figures 10–11) and their contributions to the total variances shown in figure 12. The mode profiles also show that the internal boluses on shelf have a large second-mode contribution. These results indicate that some energy in the incident mode-one wave has gone into the second-mode and is transmitted onshelf, while the reflected energy is almost exclusively in the first-mode.

3.3. *Bolus formation*

From a qualitative perspective, the diagnostics using the velocity and density fields have revealed the formation of upslope-surging blobs of fluid that form as internal boluses onshelf. However, in order to quantitatively investigate the conditions under which the surging fronts occur, we explore a wide parameter space that covers a range of values of γ/s spanning subcritical to supercritical slopes as well as Fr ranging from low to high values to quantify the effects of nonlinearity. As outlined in table 1, we have performed simulations for ten different values of γ/s and four different Fr. We also carried out additional runs to cover the gaps in the data for intermediate Fr for a subset of slope ratios, namely $\gamma/s = 0.5, 0.75, 1.0, 1.2$ and 1.5, as shown in table 1.

We assess the formation of an internal bolus by determining the vertical displacement Δz of the densest fluid onshelf from its equilibrium position offshelf as

$$\frac{\Delta z}{D} = \frac{(z_{max(\rho)_{onshelf}} - z_{eq})}{D}, \tag{3.1}$$

where $z_{max(\rho)_{onshelf}}$ is the elevation of the densest fluid onshelf over the entire duration of the simulation, and z_{eq} is the offshelf equilibrium elevation of $\max(\rho)_{onshelf}$ given

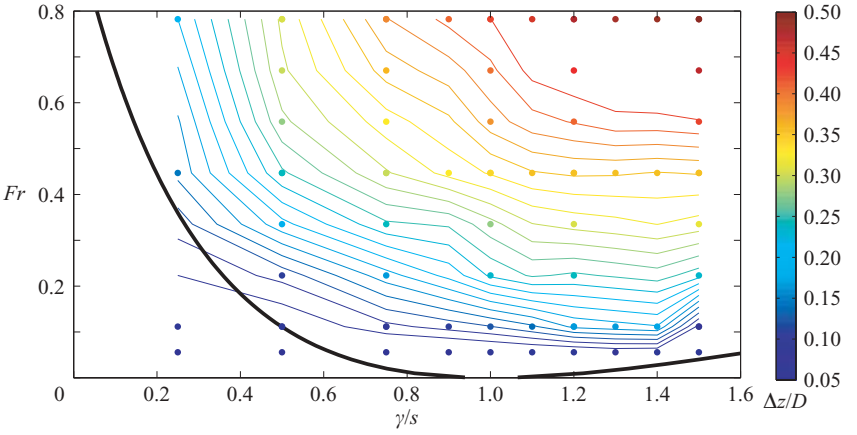

FIGURE 13. Contour plot interpolated from data points (filled circles) showing the region where formation of the internal bolus in the γ/s – Fr space can occur. The normalized vertical displacement $\Delta z/D$, of the densest fluid onshelf (calculated using equation (3.1)) is used as a measure of the formation of a bolus (shown in colour here). The curved line indicates the lower bound predicted by linear theory for the formation of bores/boluses as given by equations (3.7).

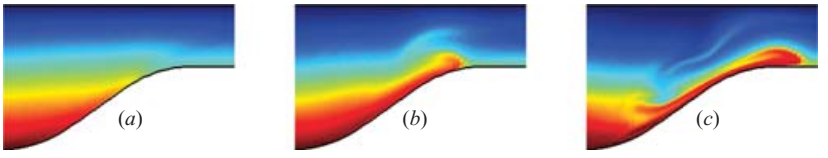

FIGURE 14. Density contours at the shelf break for critical slope ($\gamma/s = 1$) at time $t/T = 5.6$ for (*a*) $Fr = 0.11$, (*b*) $Fr = 0.45$ and (*c*) $Fr = 0.78$, respectively.

by

$$z_{eq} = -\frac{(\max(\rho)_{onshelf} - \rho_0)}{\Delta\rho} D, \tag{3.2}$$

where D is the offshore water depth and $\Delta\rho/\rho_0 = 0.02$. The results obtained from such an analysis are shown as a contour plot in figure 13 in the γ/s–Fr space, and the $\Delta z/D$ values are shown as coloured circles. When Fr is small (linear incoming waves), the waves transmit/reflect as shallow internal modes without any significant distortion of isopycnals and formation of boluses (i.e. the vertical diplacement Δz is small and comparable to the amplitude of the incoming wave). As Fr increases, heavy fluid is lifted up over greater vertical displacements for all slopes as would be expected. For example, the density contours shown in figure 14 indicate the trend at the critical slope of $\gamma/s = 1$, for $Fr = 0.11$, 0.45 and 0.78, corresponding to linear, nonlinear and highly nonlinear cases, respectively. For the linear case ($Fr = 0.11$), there is no evidence of a bolus at the shelf break, whereas the presence of a bolus is seen more prominently as Fr increases (see figure 14*b*, *c*). This indicates that the formation of boluses across the shelf break is strongly dependent on Fr and their formation leads to a relatively high value of $\Delta z/D$. For a given Fr, it is seen that the vertical displacements are higher for slopes close to critical for the cases we have explored, with Δz decreasing faster for subcritical slopes than for supercritical slopes.

We can calculate the lower bound for the formation of bores and/or boluses using a prediction from linear theory on the reflection of finite-amplitude internal waves

using the approach of Legg & Adcroft (2003). They use the criteria that the advective velocity should exceed the phase velocity of the reflected wave for a bore or a thermal front to develop. Hence, we could suppose that $Fr > 1$ for the reflected wave is a necessary condition for a front to develop. From linear theory, it is known that the frequencies of the incident and reflected waves are conserved upon reflection, which implies that the angles of inclination of the two wavenumbers k_i and k_r of the incident and reflected waves, respectively, to the vertical must be equal (see Phillips 1977). This gives the horizontal wavenumber of the reflected wave as

$$k_r = k_i \frac{\sin(\alpha + \theta)}{\sin(|\alpha - \theta|)}, \tag{3.3}$$

where α is the angle of the wave characteristic with respect to the horizontal as defined in equation (1.1) and θ is the angle of the topographic slope with respect to the horizontal (see figure 1). This implies that the horizontal phase velocity of the reflected wave is less than that of the incoming wave (for $0 < |\alpha - \theta| < \pi/2$), and is given by

$$(c_{ph})_r = \frac{\omega}{k_i} \frac{\sin(\alpha - \theta)}{\sin(|\alpha + \theta|)}. \tag{3.4}$$

Note that the reflection is regular with $k_i = k_r$ for $\theta = 0$ or $\pi/2$ (i.e. when the topographic slope is either horizontal or vertical). Since the energy density of the reflected wave increases upon reflection, it can be shown that the velocity amplitude of the reflected wave increases and is given by

$$(U_0)_r = (U_0)_i \frac{\sin(\alpha + \theta)}{\sin(|\alpha - \theta|)}. \tag{3.5}$$

From equations (3.3)–(3.5), it is easy to show that the Froude number of the reflected wave enhances to

$$Fr_r = \frac{(U_0)_r}{(c_p)_r} = \frac{(U_0)_i}{(c_p)_i} \left(\frac{\sin(\alpha + \theta)}{\sin(|\alpha - \theta|)} \right)^2. \tag{3.6}$$

Legg & Adcroft (2003) derive the range of values of topographic slopes $\gamma = \tan\theta$, that define the region for which $Fr_r > 1$ by rewriting equation (3.6) as a function of the incoming wave parameters. We rewrite these relationships in terms of γ/s as follows:

$$(\gamma/s)_1 = \frac{Fr_i^{-1/2} - 1}{Fr_i^{-1/2} + 1}, \qquad (\gamma/s)_2 = \frac{Fr_i^{-1/2} + 1}{Fr_i^{-1/2} - 1}, \tag{3.7}$$

where $(\gamma/s)_1 < 1$ defines the subcritical region while $(\gamma/s)_2 > 1$ defines the supercritical region. The boundary between these two regions is plotted in figure 13 as a curved solid line. The formation of boluses does not occur immediately above this line as can be seen (for example) in figure 14. However, it is important to recall that this theory predicts only the formation of the bores onslope and here we are extending it to examine the actual occurrence of boluses further up onshelf. Therefore, it suffices to say that the theory provides an estimate of the lower boundary for the formation of boluses. Furthermore, this theory applies to linear inviscid waves, and we expect viscosity to increase the critical Froude number at which boluses form for a given γ/s.

While figure 13 provides an assessment of the formation of internal boluses, the strength of an internal bolus can be obtained by quantifying the mass of a rectangular

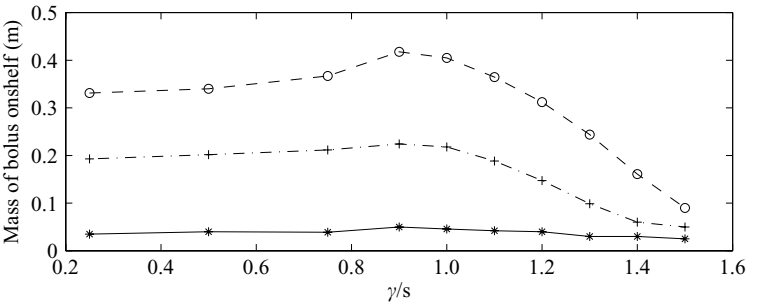

FIGURE 15. The non-dimensional mass of the bolus core (calculated using equation (3.8)) on the shelf as a function of γ/s for $Fr = 0.11$ ($\star$), $Fr = 0.45$ (+) and $Fr = 0.78$ ($\circ$), respectively.

control volume of fixed width $(1/2)D$ and depth d_S, containing the bolus, as follows

$$m = \max\left(\int_V (\rho - \rho_b)\,\mathrm{d}V \Big/ \int_V \rho_b\,\mathrm{d}V\right), \tag{3.8}$$

where ρ is the density of the fluid within the control volume during the passage of the bolus, and ρ_b is the density of the ambient fluid in the control volume. The left-hand boundary of the control volume is located at the beginning of the shelf break while the right-hand boundary is at a distance of $D/2$ shoreward from the shelf break. Equation (3.8) provides a normalized measure of the nonlinear mass transported onshelf by the bolus. Figure 15 shows the results obtained using equation (3.8) for $Fr = 0.11$, 0.45 and 0.78, as a function of γ/s. For $Fr = 0.11$, the mass transported is relatively small and a weak function of γ/s. As Fr increases, the mass transported increases significantly, especially for subcritical and near-critical slopes. It is seen that the boluses are stronger for slopes close to critical for these highly nonlinear cases, with the strength of the boluses decreasing faster for supercritical slopes than for subcritical slopes. To ascertain whether this is always the case is not trivial since (as discussed earlier) there is an additional parameter that also controls this process, namely the 'tallness' (or amplitude) of the topography given by the ratio $(D - d_s)/D$. However, isolating the effects of $(D - d_s)/D$ from γ/s is difficult since both of these parameters are implicitly linked in finite-depth domains, such as the present problem. We believe there is no unique way of obtaining different values of γ/s without altering the tallness parameter or changing the properties of the incoming wave field.

4. Onshelf dynamics of internal boluses

The nonlinear internal boluses transport dense fluid as they propagate onshelf. Therefore, an understanding of their propagation properties as well as their internal structure is desirable. In what follows, we consider the propagation of a typical well-developed nonlinear internal bolus (which would occur at high Fr) such as the one depicted in figure 2(f) and analyse its propagation speed as well as its internal structure.

4.1. *Bolus propagation speed*

Figure 16 (a) shows a detail of the internal bolus shown in figure 2(f), where we have superposed the velocity field over the density field. A bolus speed U_b can be defined as the speed at which the foremost point (the nose) of the bolus travels (this is a common way of defining front speeds of gravity currents, see e.g. Simpson 1972;

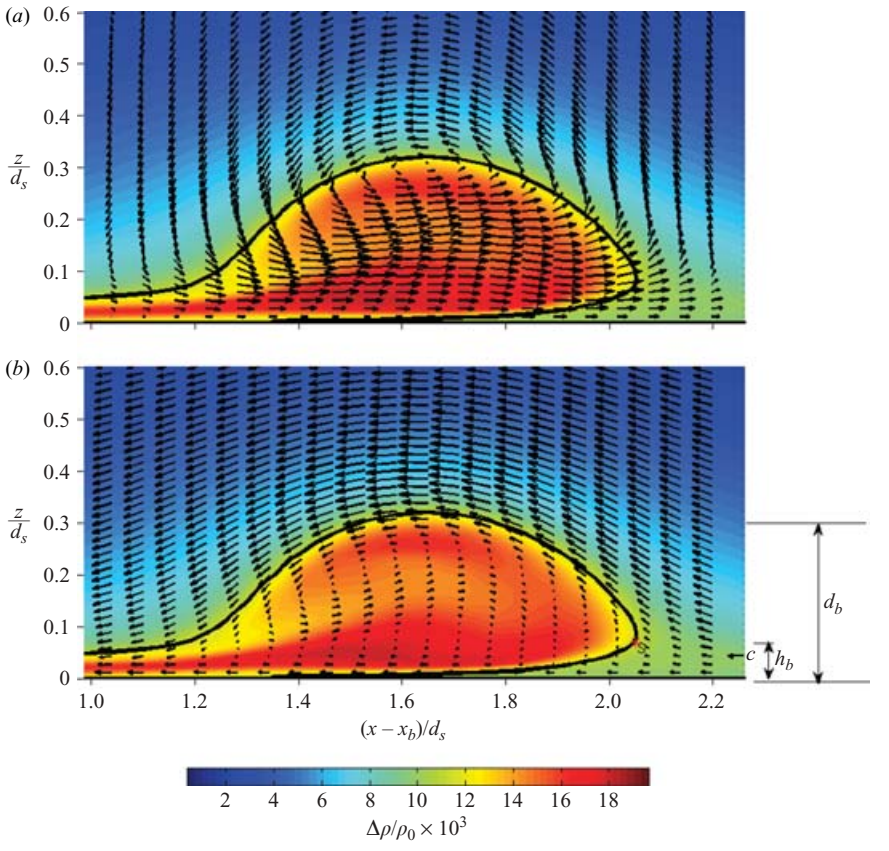

FIGURE 16. Velocity vectors superimposed on the density contours in (*a*) a stationary reference frame to show the amplification of onshore velocities at bolus locations, and (*b*) a frame that moves with the wave to the right at speed c, showing the circulation within the core of the bolus. This figure is an enlarged detail of the bolus shown in figure 2 at time $t/T = 5.8$. The scale of the phase speed/bolus front speed is shown by the vector in the bottom right of (*b*), where at this time $c = U_b = 5.4\,\mathrm{cm\,s^{-1}}$. The cross-shore distances are measured from the shelf break. All distances have been normalized by the shelf water depth d_s. S denotes the stagnation point; h_b and d_b denote the heights of the stagnation point and the top of the bolus above the lower boundary, respectively. Every other velocity vector is depicted for clarity.

Härtel, Meiburg & Necker 2000), i.e.

$$U_b = \frac{\mathrm{d}x_b}{\mathrm{d}t}, \tag{4.1}$$

where x_b denotes the actual position of the nose of the bolus in the cross-shore direction. The position of the nose as a function of time can be determined easily by inspection of the density fields. We use a backward Euler approximation to calculate U_b as a function of time (figure 17). An efficient method for computing U_b given only the instantaneous velocity and density fields (as would be the case for data obtained from field measurements) is to compute a phase speed c that minimizes the time rate of change of the density field in a reference frame that moves with the wave (Fringer & Street 2003). In this moving frame, the streamlines will be parallel to the lines of constant density and c should therefore provide a good estimate of the bolus propagation speed U_b. Fringer & Street (2003) indicate that a global measure of this

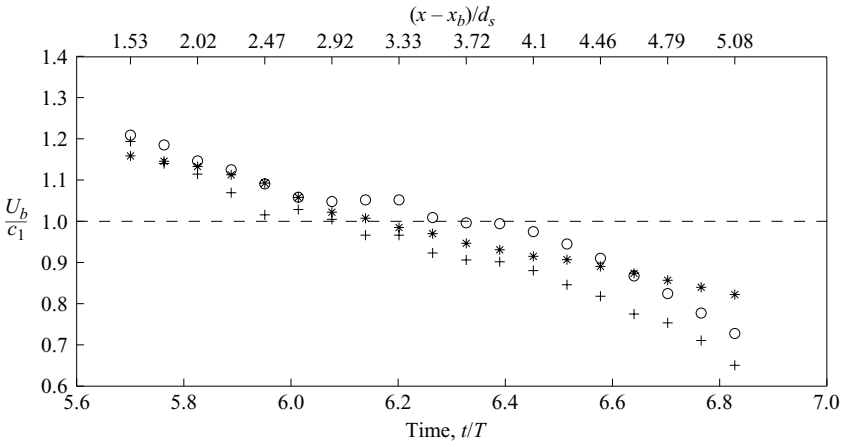

FIGURE 17. The speed of propagation of an internal bolus, U_b, as a function of time for a critical slope with $Fr = 0.783$ normalized by the first-mode phase speed c_1. +, phase speed U_b/c_1 computed from the propagation distance of the nose of the bolus in time given by equation (4.1); ∘, phase speed c/c_1 computed by minimizing the time-rate of change of the density field given by equation (4.3); *, the front speed from the empirical relationship of Maxworthy *et al.* (2002), given by equation (4.5). The top x-axis shows the distance of the nose of the bolus from the shelf break normalized by the shelf water depth d_s.

time rate of change in a frame moving at speed c is given by the 2-norm

$$E_2^2(c) = \int_V \left(\frac{\partial \rho}{\partial t}\right)^2 \mathrm{d}V = \int_V \left[(u-c)\frac{\partial \rho}{\partial x} + w\frac{\partial \rho}{\partial z}\right]^2 \mathrm{d}V, \tag{4.2}$$

where V represents the volume of the computational domain containing the bolus. The phase speed c can then be obtained by differentiating equation (4.2) with respect to c, resulting in a phase speed that minimizes $E_2(c)$,

$$c = \int_V (u\rho_x + w\rho_z)\rho_x \,\mathrm{d}V \Big/ \int_V \rho_x^2 \,\mathrm{d}V. \tag{4.3}$$

The velocity field in a translating system moving at this speed c indicates that the flow aligns well with the isopycnals (figure 16*b*). As shown in figure 18, the streamlines in this moving frame clearly demonstrate the bifurcation of the flow around the nose of the bolus. The phase speed calculated using (4.3) is plotted in figure 17 as a function of time, and the results show how the minimization technique is consistently 5–10 % higher than U_b given by (4.1). This is because (4.3) assumes an inviscid flow field, which is slightly inaccurate owing to the presence of the boundary layer that results in the formation of a non-propagating tail at the rear end of the bolus.

Figure 17 shows that the bolus slows down significantly within one wave period. During this period the bolus shrinks, as it loses its initial mass continuously owing to drainage of dense fluid from the rear of the bolus as depicted by the time sequence in figure 19. In the simplest and intuitive view, it appears that the bolus propagates as a gravity current driven by a buoyancy force due to the presence of a density contrast,

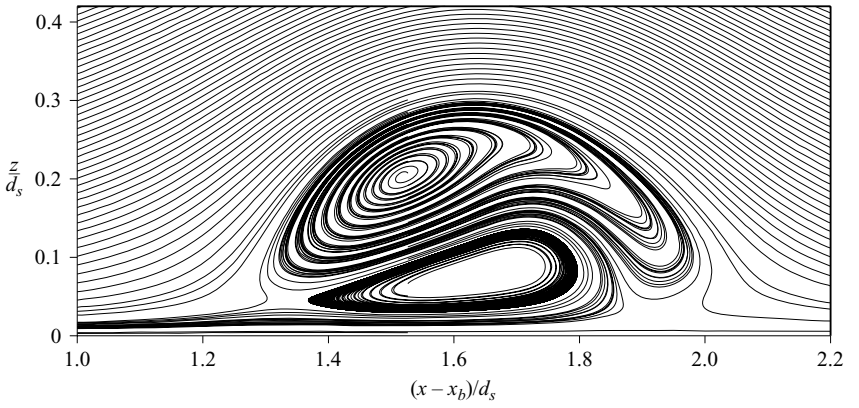

FIGURE 18. Streamlines in a frame that moves with the wave to the right at speed c, showing the circulation within the core of the bolus at time $t/T = 5.8$.

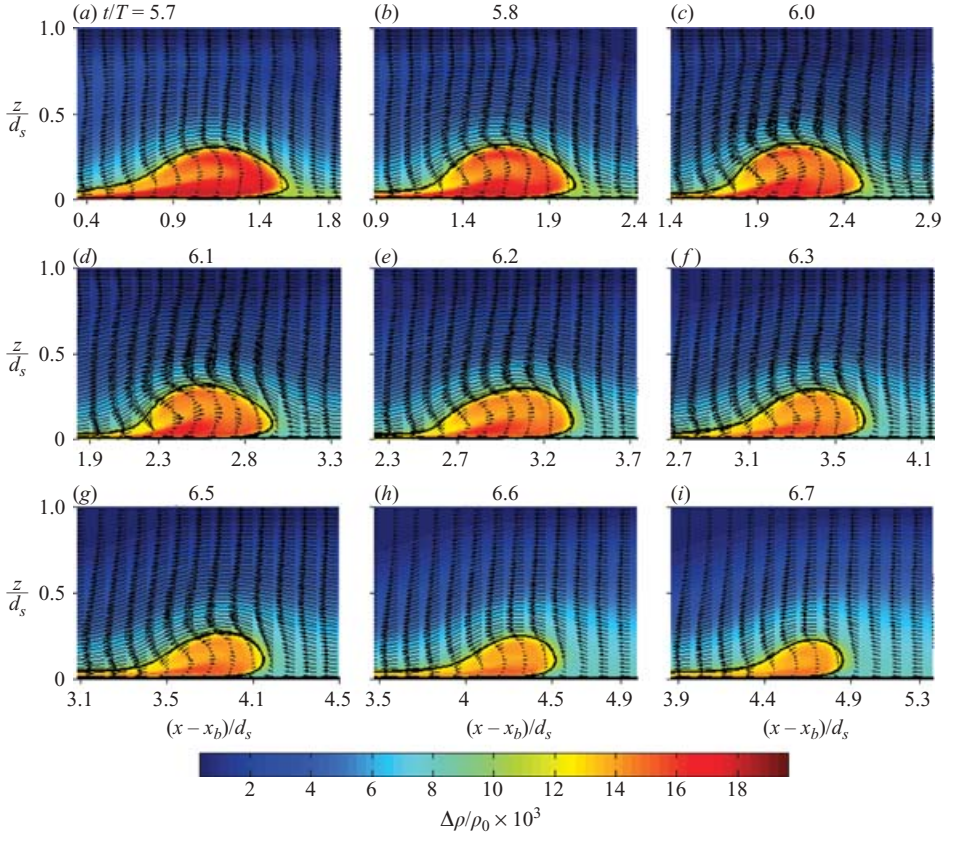

FIGURE 19. Time sequence showing the propagation of an internal bolus in a frame that moves with the wave to the right at speeds U_b, given in figure 17. The cross-shore distances are measured from the shelf break. All distances have been normalized by the shelf water depth d_s, and every other velocity vector is depicted for clarity.

which diminishes as the bolus loses its mass and amplitude. The propagation speed of the bolus can be compared to the onshelf speed of propagation of a linear hydrostatic first-mode internal wave $c_1 = Nd_s/\pi$ (shown as a dashed line in figure 17), and here we define the ratio U_b/c_1 as the bolus Froude number Fr_b. Initially and for up to a distance of nearly $3d_s$ from the shelf break (where d_s is the onshelf water depth), the speed of the bolus is greater than c_1 (i.e. $Fr_b > 1$), a situation that is often described as supercritical in the propagation of gravity currents (Long 1955; Maxworthy *et al.* 2002). During this phase of its propagation, the bolus maintains its shape. However, later in time, as the bolus passes through the critical point ($Fr_b = 1$, see figure 19*e* and beyond, the shape of the bolus changes significantly as it begins to dissipate rather rapidly and propagates subcritically (when $Fr_b < 1$). The three-dimensional density isosurfaces shown in figure 3 give us insight into what happens during this period. In figures 3(*d*)–3(*g*), it can be seen that there are no noticeable lateral variations in the structure of the bolus. On the other hand, the presence of lateral instabilities can be seen in figure 3(*h*), and these instabilities intensify in figure 3(*i*, *j*). Soon after they cause the bolus to break down into longitudinal vortices which dissipate rapidly (not shown). We speculate that the mechanism behind this instability is similar to that which causes the classical lobe and cleft instability in gravity currents flowing over a no-slip boundary, where heavy fluid overruns light fluid and results in a Rayleigh–Taylor instability (for a detailed discussion, see Simpson 1972, 1997).

The scaling of the propagation of gravity currents in a linearly stratified ambient fluid has been investigated experimentally and numerically by Maxworthy *et al.* (2002) and analytically for the inviscid case by Ungarish (2006). Maxworthy *et al.* (2002) define a parameter R given by

$$R = \frac{(\rho_c - \rho_0)}{(\rho_b - \rho_0)}, \tag{4.4}$$

where ρ_c is the initial density of the current, and ρ_b is the density at the bottom of the linearly stratified water column. The ratio R hence provides a measure of the strength of the current $(\rho_c - \rho_0)$ relative to the strength of stratification $(\rho_b - \rho_0)$. They provide functional relationships for the Froude number as a function of R (see figure 7 of their paper) for different ratios of the gravity current depth h to the water depth H. For the bolus shown in figure 19, the ratio is initially close to $1/3$ for which they provide the relationship for the Froude number $Fr_m = V_b/NH$, as a function of R as

$$Fr_m = 0.147 + 0.774 \log(R), \tag{4.5}$$

where V_b is the front propagation speed, N is the buoyancy frequency of the stratified water column and H is the total water depth. The values of the bolus front speed obtained using equation (4.5) are shown in figure 17. The agreement is remarkable, especially when the flow is still supercritical. However, when the bolus is in the subcritical regime, the speeds predicted by their relationship begin to deviate from the general trend of the computed speeds outlined earlier. This is not so surprising since the ratio h/H becomes much less than a third, below which equation (4.5) is not valid. We also carried out a comparison of our results with the inviscid analytic results given by Ungarish (2006) (not shown here). We find that the inviscid theory predicts speeds that are at least 50 % higher than our speeds, possibly because of effects of low Reynolds number in our simulations as well as the presence of the no-slip boundary which is not accounted for in an inviscid analysis. This is consistent with the findings

of Härtel *et al.* (2000), where they note that the *Fr* is higher for currents flowing over slip boundaries, although the differences decrease with increasing Grashof numbers *Gr*, which plays the role of a Reynolds number in their case.

4.2. *Structure of an internal bolus*

A typical snapshot of an internal bolus as depicted in figure 16(*a*) shows a striking resemblance to the head of a gravity current flowing over a no-slip lower boundary (see Simpson 1972; Simpson & Britter 1979). The nose of the bolus is raised slightly above the bottom wall and in a frame moving with the bolus as shown in figure 16(*b*), a stagnation point occurs at the nose around which the flow divides.

Figures 16(*b*) and 18 provide a better perspective of the circulation dynamics within the interior of the bolus core as well as its immediate surroundings. The streamlines in this moving reference frame as depicted in figure 18 show two circulation regions within the bolus: the first is the more pronounced circulation in the upper part of the bolus head where the circulation speeds are of order U_b as seen from figure 16(*b*). In addition to this main circulation, a reverse smaller circulation occurs close to the lower boundary that causes dense fluid to drain through the rear of the bolus. This small layer of dense fluid draining at the lower end of the bolus (as shown in figure 16*b*) can be thought of as another gravity current flowing in the reverse direction (offshore) to the main current flowing onshore. The flow features observed here are very similar to the flow characteristics of a typical gravity current head as described by Simpson (1972, 1997) from his classical laboratory experiments of gravity currents. Simpson (1972) provides an empirical scaling for the nose height as

$$h_b/d_b = 0.61\, Re_b^{-0.23}, \tag{4.6}$$

where h_b is the height of the nose above the bottom, d_b is the maximum height of the bolus (see figure 16*b*) and $Re_b = U_b d_b/\nu$ is the bolus Reynolds number. For the bolus shown in figure 16, using a bolus front speed of $U_b = 0.054\,\mathrm{m\,s^{-1}}$ and $d_b = 80\,\mathrm{mm}$, with $\nu = 10^{-5}\ \mathrm{m^2\ s^{-1}}$, gives $h_b/d_b \simeq 0.15$, compared to the actual ratio which is nearly 0.2. This is within the range of scatter of the data showing the variation of the nose height as a function of Reynolds number in the work of Simpson & Britter (1979).

It is clear that there is a strong circulation region within the bolus. Furthermore, the interaction of the incident wave with the slope generates a great deal of vorticity. In order to determine whether the flow field contains vortex cores in both the slope region as well as within the bolus, we use the λ_2 method of Jeong & Hussain (1995), which is an attractive and robust method for visualizing vortices. The method essentially seeks a measure of the low pressure that exists inside a vortex. This is achieved by calculating the median eigenvalue λ_2 of the tensor, $(S_{ik}S_{kj} + \Omega_{ik}\Omega_{kj})$, where S_{ij} is the strain-rate (symmetric) tensor and Ω_{ij} is the rotation (antisymmmetric) tensor. Since the tensor $(S_{ik}S_{kj} + \Omega_{ik}\Omega_{kj})$ is symmetric, it has only real eigenvalues (with $\lambda_1 \geqslant \lambda_2 \geqslant \lambda_3$). Hence, a vortex core can be defined as a zone where $\lambda_2 < 0$ (for a detailed discussion, see Jeong & Hussain 1995). Figure 20 shows the instantaneous isosurfaces of λ_2 at time $t/T = 5.8$ for the bolus shown in figure 16. This figure shows that the interaction process generates an intense vortex of dense fluid in the slope region that moves upslope. Within the bolus itself, a larger vortex core exists in the region where the strong upper circulation occurs and a smaller vortex core exists close to the nose where the lower reverse weaker circulation occurs. This is more clearly seen in the side view showing contours of λ_2 superimposed over the density field as depicted in figure 21.

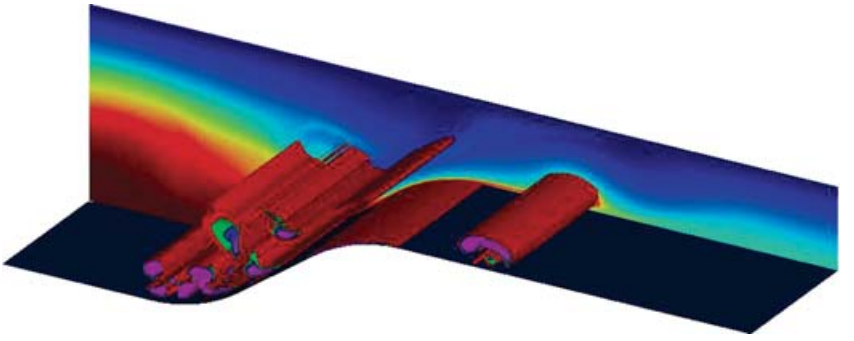

FIGURE 20. Instantaneous snapshot of vortex cores plotted as isosurfaces of $\lambda_2 < 0$. The isosurfaces shown are $\lambda_2 = -0.1, -0.2, -0.3$ and -0.5, respectively. $t/T = 5.8$.

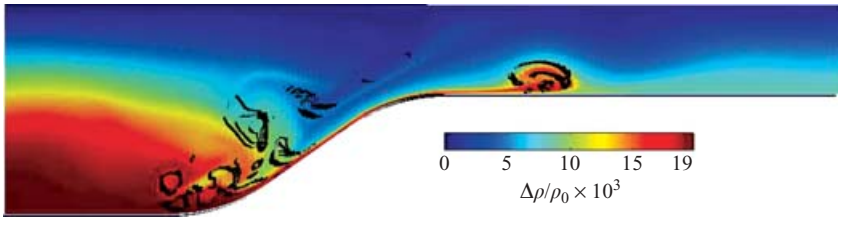

FIGURE 21. Side view of figure 20 showing contours of $\lambda_2 < 0$ (in black) superimposed over the density field indicating the vortex cores onslope and within the bolus. $t/T = 5.8$.

5. Concluding remarks

There have been many recent observations of nonlinear internal waves of elevation in coastal waters, but it is not clear exactly what these features are with regard to their generation mechanism, propagation and dissipation. This paper describes for the first time a detailed study showing results on how internal waves interacting with sloping boundaries lead to the formation of internal boluses. We have presented results from highly resolved numerical simulations of the interaction of first-mode internal gravity waves with a shelf break in two- and three-dimensional flows. The emphasis of this study was to obtain an understanding of the interaction dynamics at the slope leading to the formation of upslope-surging fronts of dense fluid that are ejected onshelf as internal boluses.

Flow fields in the slope region reveal the complex flow patterns that occur when highly nonlinear incident first-mode internal waves interact and reflect off the slope and lead to the generation of internal boluses. Modal analysis results indicate the generation of higher-mode waves when the mode-one incident wave field interacts with the slope. There is a significant amount of wave energy in the second-mode at the midslope region, which is transmitted onshelf by the internal boluses, while the reflected energy offshore is exclusively in the first-mode. The strength of these boluses enhances monotonically with the Froude number Fr, and the bolus formation data shows that linear theory provides a lower bound for the region in which boluses form (see figure 13). Furthermore, for an incoming highly nonlinear wave, the mass transported by the bolus is optimal for slopes close to critical.

A detailed analysis of the propagation speeds of a typical internal bolus shows that they essentially follow the scaling dynamics of gravity currents. The results in this

paper demonstrate that there is reasonable agreement with predictions of speeds given by Maxworthy *et al.* (2002) from their study of gravity currents in linearly stratified fluids. The results also show that a bolus loses its mass faster once it transitions from supercritical propagation to subcritical propagation, at which time three-dimensional lateral instabilities become apparent. The circulation pattern within the core of the bolus contains a strong upper circulation region with a lower reverse circulation region that is very similar to the circulation observed in the head of a gravity current flowing over a no-slip boundary. A three-dimensional simulation of the flow shows the presence of closed cores (vortex cores) in the upper part of the internal bolus where the main circulation is observed. The development of the classical lobe and cleft instability at the nose of the bolus also occurs.

One view based on the present study is that the interaction of low-mode internal waves with bathymetry can lead to the formation of boluses containing energy from higher modes that have propagation properties similar to gravity currents. Discussion of the mixing and dissipation resulting from the interaction process at the slope as well as onshelf is left to a subsequent paper based on results from three-dimensional simulations.

The authors thank the three anonymous referees for their useful comments and recommendations. We gratefully acknowledge the support of the Leavell Family Faculty Scholarship in the Department of Civil and Environmental Engineering at Stanford University and ONR grant N00014-05-1-0294 (Scientific officers: Dr C. Linwood Vincent, Dr Terri Paluszkiewicz and Dr Scott Harper).

REFERENCES

Borzelli, G. & Ligi, R. 1999 Empirical orthogonal function analysis of sst image series: a physical interpretation. *J. Phys. Oceanogr.* **16**, 682–690.

Cacchione, D. & Wunsch, C. 1974 Experimental study of internal waves over a slope. *J. Fluid Mech.* **66**, 223–239.

Carter, G. S., Gregg, M. C. & Lien, R.-C. 2005 Internal waves, solitary waves, and mixing on the Monterey Bay shelf. *Continental Shelf Res.* **25**, 1499–1520.

Craig, P. D. 1985 Internal wave dynamics over coastal topography. PhD thesis, University of Western Australia.

Cui, A. & Street, R. L. 2001 Large-eddy simulation of turbulent rotation convective flow development. *J. Fluid Mech.* **447**, 53–84.

Cui, A. & Street, R. L. 2004 Large-eddy simulation of coastal upwelling flow. *Environ. Fluid Mech.* **4**, 197–223.

Dauxois, T., Didier, A. & Falcon, E. 2004 Observation of near-critical reflection of internal waves in a stably stratified fluid. *Phys. Fluids* **16**, 1936–1941.

Dauxois, T. & Young, W. R. 1999 Near-critical reflection of internal waves. *J. Fluid Mech.* **390**, 271–295.

Fringer, O. B. & Street, R. L. 2003 The dynamics of breaking progressive interfacial waves. *J. Fluid Mech.* **494**, 319–353.

Härtel, C., Meiburg, E. & Necker, F. 2000 Analysis and direct numerical simulation of the flow at a gravity-current head. Part 1. Flow topology and front speed for slip and no-slip boundaries. *J. Fluid Mech.* **418**, 189–212.

Ivey, G. N. & Nokes, R. I. 1989 Vertical mixing due to the breaking of critical internal waves on sloping boundaries. *J. Fluid Mech.* **204**, 479–500.

Ivey, G. N., Winters, K. B. & De Silva, I. P. D. 2000 Turbulent mixing in a sloping benthic boundary layer energized by internal waves. *J. Fluid Mech.* **418**, 59–76.

Jeong, J. & Hussain, F. 1995 On the identification of a vortex. *J. Fluid Mech.* **285**, 69–94.

Klymak, J. M. & Moum, J. N. 2003 Internal solitary waves of elevation advancing on a shoaling shelf. *Geophys. Res. Lett.* **30**, 2045.

Kundu, P. K. 1990 *Fluid Mechanics*. Academic.

Kunze, E. & Llewellyn Smith, S. G. 2004 The role of small-scale topography in turbulent mixing of the global ocean. *Oceanography* **17**, 55–64.

Legg, S. & Adcroft, A. 2003 Internal wave breaking at concave and convex continental slopes. *J. Phys. Oceanogr.* **33**, 2224–2246.

Long, R. R. 1955 Some aspects of the flow of stratified fluids, III. Continuous density gradients. *Tellus* **7**, 341–357.

Maxworthy, T., Leilich, J., Simpson, J. E. & Meiburg, E. 2002 The propagation of a gravity current into a linearly stratified fluid. *J. Fluid Mech.* **453**, 371–394.

Munk, W. & Wunsch, C. 1998 Abyssal recipes II: energetics of tidal and wind mixing. *Deep-Sea Res.* **45**, 1977–2010.

Nash, J. D., Kunze, E., Toole, J. M. & Schmitt, R. W. 2004 Internal tide reflection and turbulent mixing on the continental slope. *J. Phys. Oceanogr.* **34**, 1117–1134.

Phillips, O. M. 1977 *The Dynamics of the Upper Ocean*. Cambridge University Press.

Simpson, A. E. 1972 Effects of the lower boundary on the head of a gravity current. *J. Fluid Mech.* **53**, 759–768.

Simpson, A. E. 1997 *Gravity Currents*. Cambridge University Press.

Simpson, A. E. & Britter, R. E. 1979 The dynamics of the head of a gravity current advancing over a horizontal surface. *J. Fluid Mech.* **94**, 477–495.

Slinn, D. N. & Riley, J. J. 1998 Turbulent dynamics of a critically reflecting internal gravity wave. *Theor. Comput. Fluid Dyn.* **11**, 281–303.

Taylor, J. R. 1993 Turbulence and mixing in the boundary layer generated by shoaling internal waves. *J. Fluid Mech.* **19**, 233–233.

Thorpe, S. A. 1987 On the reflection of a strain of finite-amplitude internal waves from a uniform slope. *J. Fluid Mech.* **178**, 279–302.

Thorpe, S. A. 1992 Thermal fronts caused by internal gravity waves reflecting from a slope. *J. Phys. Oceanogr.* **22**, 105–108.

Thorpe, S. A. 1999 The generation of alongslope currents by breaking internal waves. *J. Phys. Oceanogr.* **29**, 29–45.

Ungarish, M. 2006 On gravity currents in a linearly stratified ambient: a generalization of Benjamin's steady-state propagation results. *J. Fluid Mech.* **548**, 49–68.

Venayagamoorthy, S. K. & Fringer, O. B. 2005 Nonhydrostatic and nonlinear contributions to the energy flux budget in nonlinear internal waves. *Geophys. Res. Lett.* **32**, L15603.

Venayagamoorthy, S. K. & Fringer, O. B. 2006 Numerical simulations of the interaction of internal waves with a shelf break. *Phys. Fluids* **18**(7), 076603.

Zang, Y. & Street, R. L. 1995 Numerical simulation of coastal upwelling and interfacial instability in a rotating and stratified fluid. *J. Fluid Mech.* **305**, 47–75.

Zang, Y., Street, R. L. & Koseff, J. R. 1994 A non-staggered grid, fractional step method for time-dependent incompressible Navier–Stokes equations in curvilinear coordinates. *J. Comput. Phys.* **114**, 18–33.

Zedler, E. A. & Street, R. L. 2001 Large-eddy simulation of sediment transport: currents over ripples. *J. Hydraul. Engng ASCE* **127**, 442–452.